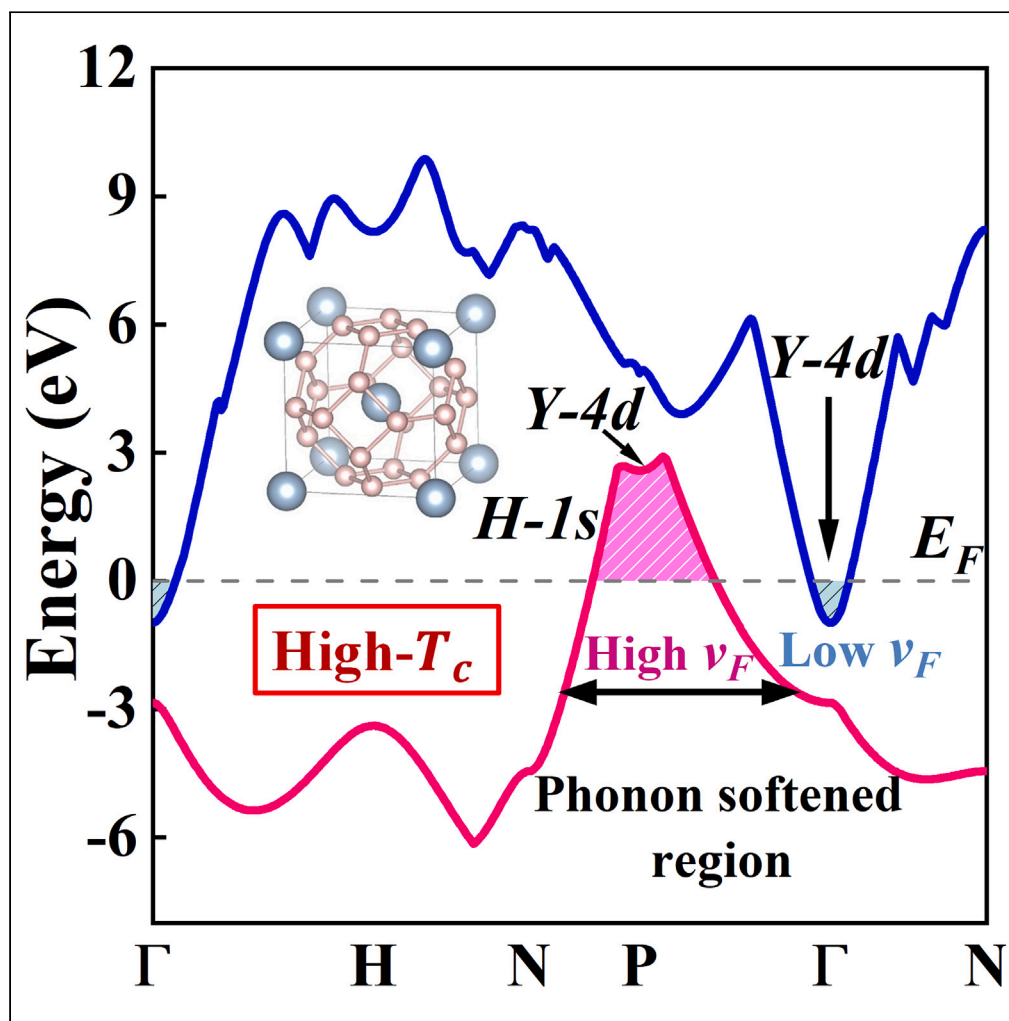## Article

Emerging superconductivity rules in rare-earth and alkaline-earth metal hydrides

Ya-Le Tao, Qi-Jun Liu, Dai-He Fan, Fu-Sheng Liu, Zheng-Tang Liu

qijunliu@home.swjtu.edu.cn

Highlights
This paper discovers new high-temperature superconductivity rules

d-orbital electrons change the Fermi surface and open the superconducting gap

YH_6 has strong EPC-induced CDW order and T_c up to 230K, an excellent superconductor

Double gap and EPC in phonon softening regions for high T_c hydrides

Article

Emerging superconductivity rules in rare-earth and alkaline-earth metal hydrides

Ya-Le Tao,[1] Qi-Jun Liu,[1,3,*] Dai-He Fan,[1] Fu-Sheng Liu,[1] and Zheng-Tang Liu[2]

SUMMARY

Hydrides of alkaline-earth and rare-earth metals have garnered significant interest in high-temperature superconductor research due to their excellent electron-phonon coupling and high T_c upon pressurization. This study explores the electronic structures and electron-phonon coupling of metal hydrides XH_n (n = 4,6), where X includes Ca, Mg, Sc, and Y. The involvement of d-orbital electrons alters the Fermi surface, leading to saddle-point nesting and a charge density wave (CDW) phase transition, which opens the superconducting gap. For instance, in YH_6, the exchange coupling between Y-4d and H-1s holes in the phonon softening region results in T_c values up to 230 K. The study suggests that factors, such as the origin of the CDW order, hydrogen concentration, and d-orbital contributions are crucial to superconductivity. This work proposes a new rule for high T_c superconductors, emphasizing the importance of double gaps and electron-phonon interactions at exchange coupling sites, and predicts potential high-quality superconductors among rare-earth hydrides.

INTRODUCTION

Realizing room temperature superconductivity is the eventual target of superconductivity characterization studies. For the simplest element-hydrogen, it has been predicted that metallic hydrogen may become an ideal high-temperature superconductor because it possesses a light mass and high frequency.[1] Theoretically, it is possible to dissociate hydrogen molecules under pressure and thus achieve metallization. The weakening of molecular bonds accompanied by an increase in pressure was found in the high-pressure phase diagram of hydrogen.[2] So, it is theoretically possible to synthesize metallic hydrogen under high pressure. A number of recent experimental studies have proposed the thesis of hydrogen metallization,[3–7] because the hydrogen atom has the smallest nucleus, it shows strong moving behavior. As a result, hydrogen atoms often enter the interior of the high-pressure device diamond, thus damaging the device. Therefore, metallic hydrogen has not been successfully synthesized in experiments.

However, Ashcroft's research points out that the pressure required to convert hydrides to metals may be lower than that of pure hydrogen. This suggests that the process of hydrogen metallization may be accelerated by adding complex chemical reactions. The addition of other atoms to pure hydrogen has a "pre-compression" effect that reduces the pressure required for metallization.[8] Based on the Bardeen-Cooper-Schrieffer (BCS) theory, hydrides, as a phonon-mediated conventional superconductor that does not involve strong correlation, the Allen-Dynes formula can be used to calculate the T_c value to achieve the predicted effect.[9] In 2012, Ma et al. predicted that CaH_6 with cage structure could reach a high T_c of 215K,[10] and in 2022, the experiment successfully synthesized CaH_6.[11] The measured T_c value is basically consistent with the predicted value. Duan et al. predicted that the T_c value of H_3S at 200 GPa was 204 K in 2014,[12] and then reported that the T_c value of H_3S successfully synthesized at 155 GPa was as high as 203 K in 2015.[13] In addition, in 2017, Liu et al. predicted theoretically that the T_c of LaH_{10} could reach 274 K at 250 GPa,[14] while the T_c of LaH_{10} synthesized experimentally in 2019 could reach 260 K at 150 GPa,[15] which is the highest T_c among metal hydrides synthesized experimentally at present. In summary, it can be seen that the theoretical predicted T_c values are basically consistent with the experimental results, which indicates the reliability of the prediction of hydride superconductivity by using the traditional BCS theoretical formula. Along with this idea, scholars flocked into the study of hydride superconductivity. Hundreds of innovative hydride structures were predicted or experimentally synthesized.[16–26] New structures were obtained according to recent studies: CeH_9,[27] ThH_{10},[28] PrH_9,[29] ScH_6,[30] YH_{10},[14] AcH_{10},[31] SrH_{10},[32] HfH_{10},[33] MgH_{12},[34] and MoH_{11}.[35] Most high T_c metal hydrides are composed of metals located at the boundaries of the s/p and s/d bodies, a region known as the "instability zone", between main groups 2 and 3; the main reason for this may be the powerful electron-phonon reactions due to the small energy divergences between the orbitals.

Based on this view, we turn our attention to alkaline-earth and rare-earth metal hydrides. Notable among them is the binary hydride LaH_{10}, which is known for its T_c values of up to 260 K.[15,36,37] It consists of a three-dimensional hydrogen lattice and La atoms with a large number of hydrogen ligands around the La atoms and has been described as a stable metal-like hydrogen structure with the La atoms providing electrons to the guests. Similarly to LaH_{10}, certain alkaline-earth metal and rare-earth metals hydrides form hydrogen units under pressure, which

[1]Bond and Band Engineering Group, School of Physical Science and Technology, Southwest Jiaotong University, Chengdu 610031, People's Republic of China
[2]State Key Laboratory of Solidification Processing, Northwestern Polytechnical University, Xi'an 710072, People's Republic of China
[3]Lead contact
*Correspondence: qijunliu@home.swjtu.edu.cn
https://doi.org/10.1016/j.isci.2024.110542

contributes to the stability of the structure and is accompanied by high-temperature superconducting properties.[38] Among them, CaH_4 has a tendency to dissociate hydrogen molecules to form hydrogen atoms under pressure, but the T_c value is only 30 K.[39,40] In contrast, MgH_4 appears as a new high-pressure phase $I4/mmm$ at 255 GPa, which can reach a T_c value of 81 K.[41] Moreover, originating from the electron-phonon coupling related to the mid-frequency mode vibrations of the hydrogen atom, both ScH_4 and ScH_6 are superconducting at 200 GPa and 130 GPa, with T_c of 98 K and 129 K, respectively.[42] Analogously, CaH_6, famous for its cage-like structure, reaches a high T_c of 235 K due to the distinctive shaped square H_4 unit it forms.[10]

Although previous studies have individually reported the superconductivity of various structures, a comprehensive understanding of the mechanisms underlying high-temperature superconductivity, particularly the distinctions in superconductivity induced by hydrides of the second main group and the third subgroup, remains elusive. In order to demystify these enigmas, the hydrides represented by the elements Ca, Mg, Sc, and Y are investigated in this paper. With the use of the controlled variable method, we have systematically analyzed the impact of the metallic elements and stoichiometric number of hydrogens on the superconductivity of the second main group and third subgroup hydrides based on the variations of structural electrical properties and the electron-phonon reaction. The aim is to seek the differences in the superconductivity laws at the unstable bands and to explore where the superconductivity mechanism of different structures lies. Ultimately, a new rule for high T_c superconductivity will be proposed.

Computational methods

The calculations are proceeding by the plane wave pseudopotential method using the QUANTUM ESPRESSO package.[43–45] The optimized norm-conserving vanderbilt pseudopotentials (ONCVPSP)[46] are employed to simulate the electron-ion interaction and generalized gradient approximation (GGA-PBE) to describe the exchange and correlation potential. The wave functions cutoff and the charge density cutoff are set as 100 Ry and 400 Ry. The first Brillouin zone (BZ) is sampled by applying 36×36×36 k mesh by Gaussian smearing with a width of 0.02 Ry to perform BZ integrations. The internal atomic locations are complete relaxation with a force of critical values of 10 meV/Å. The wannier90 interpolation is utilized to estimate FSs and visualize counting results by FERMISURFER software. The phonon dispersion and electron-phonon coupling (EPC) are founded on the basis of density functional perturbation theory[47] and computed with a 9×9×9 q-point grid.

The electron-phonon interaction matrix element $g_{k,qv}^{ij}$, which determines the probability amplitude of scattering of electrons in response to crystal momentum transfer. It is determined by the following equation[48]:

$$g_{k,qv}^{ij} = \left(\frac{h}{2M_{\omega_{qv}}}\right)^{\frac{1}{2}} \left(\psi_{i,k}\left|\frac{dV_{SCF}}{d\hat{u}_{qv}} \cdot \hat{e}_{qv}\right|\psi_{j,k+q}\right) \qquad \text{(Equation 1)}$$

The phonon linewidth γ_{qv} formula is as follows:

$$\gamma_{qv} = \frac{2\pi\omega_{qv}}{\Omega_{BZ}} \sum_{ij} \int d^3k \left|g_{k,qv}^{ij}\right|^2 \delta(\epsilon_{q,i} - \epsilon_F)\delta(\epsilon_{k+q,j} - \epsilon_F) \qquad \text{(Equation 2)}$$

The modal resolution magnitude of EPC λ_{qv} is given by[49]:

$$\lambda_{qv} = \frac{\gamma_{qv}}{\pi\hbar N(e_F)\omega_{qv}^2} \qquad \text{(Equation 3)}$$

The Eliashberg electron-phonon spectral function $\alpha^2 F(\omega)$ and the EPC constant λ are calculated by

$$\alpha^2 F(\omega) = \frac{1}{2\pi N(\epsilon_F)} \sum_{qv} \delta(\omega - \omega_{qv}) \frac{\gamma_{qv}}{\hbar\omega_{qv}} \qquad \text{(Equation 4)}$$

$$\lambda = \sum_{qv} \lambda_{qv} = 2 \int \frac{\alpha^2 F(\omega)}{\omega} d\omega \qquad \text{(Equation 5)}$$

where $N(\epsilon_F)$ is the electronic DOS at the Fermi level. ω_{qv} is the phonon frequency.

The acoustic branch electron-phonon coupling constant λ_{ac} and the optical branch electron-phonon coupling constant λ_{opt} were calculated separately:

$$\lambda_{ac} = 2 \int_0^{\omega_1} \frac{\alpha^2 F(\omega)}{\omega} d\omega \qquad \text{(Equation 6)}$$

$$\lambda_{opt} = 2 \int_{\omega_1}^{\omega_{max}} \frac{\alpha^2 F(\omega)}{\omega} d\omega \qquad \text{(Equation 7)}$$

Here, ω_1 represents the maximum phonon frequency of the acoustic branch.

At last, the superconducting transition temperature is obtained by the full Allen-Dynes equation:
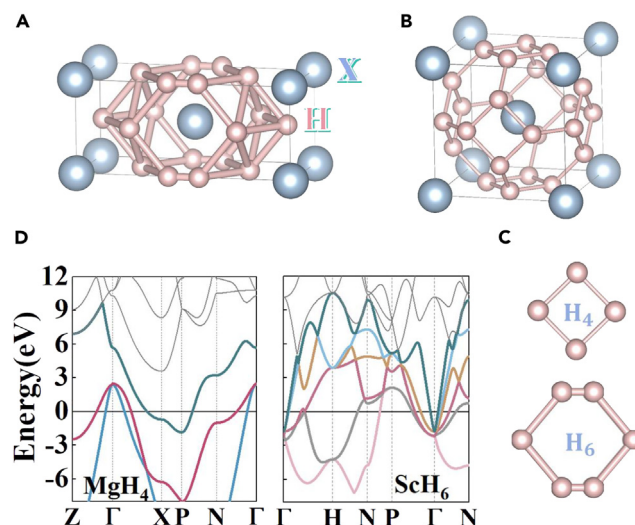
Figure 1. Crystal structure and band structure of XH$_4$ and XH$_6$

(A) Structure of XH$_4$. Here, the pink balls present hydrogen atoms, the blue balls present metal atoms (X = Ca, Mg, Sc, and Y).

(B) Structure of XH$_6$. (the element presented by atoms of different colors are same as aforementioned).

(C) H$_4$ and H$_6$ units.

(D) Band structure of MgH$_4$ and ScH$_6$. Here, MgH$_4$ has three bands crossing the Fermi energy level, while ScH$_6$ has six.

$$T_c = f_1 f_2 \frac{\omega_{\log}}{1.2} \exp\left[\frac{-1.04(1+\lambda)}{\lambda - \mu^*(1+0.62\lambda)}\right] \qquad \text{(Equation 8)}$$

Here, μ^* is the effective shielding Coulomb repulsion constant (the values taken in this article are all 0.1). $\omega_{\log}$ is logarithmic measurement average of phonon frequency.

The correction factors f_1, f_2 expressions are respectively:

$$f_1 = \left\{1 + \left[\frac{\lambda}{2.46(1+3.8\mu^*)}\right]^{\frac{3}{2}}\right\}^{\frac{1}{3}} \qquad \text{(Equation 9)}$$

$$f_2 = 1 + \frac{\left[\left(\frac{\omega_2}{\omega_{\log}}\right) - 1\right]\lambda^2}{\lambda^2 + 3.312(1+6.3\mu^*)^2\left(\frac{\omega_2}{\omega_{\log}}\right)^2} \qquad \text{(Equation 10)}$$

To account for the calculation of Fermi surface nesting, we first define the real part of the electronic susceptibility χ' as:

$$\chi'(q) = \sum_k \frac{f(\epsilon_k) - f(\epsilon_{k+q})}{\epsilon_k - \epsilon_{k+q}} \qquad \text{(Equation 11)}$$

The Fermi surface nesting function χ'', as the imaginary part of the electronic susceptibility, is defined as:

$$\lim_{\omega \to 0} X''(q, \omega)/\omega = \sum_k \delta(\epsilon_k - \epsilon_F)\delta(\epsilon_{k+q} - \epsilon_F) \qquad \text{(Equation 12)}$$

RESULTS AND DISCUSSION

Atomic structure

As illustrated in Figures 1A and 1B, the two different kinds of hydride systems are XH$_4$ and XH$_6$, where X represents Ca, Mg, Sc, and Y. It is worth noting that to ensure the credibility of the calculations, the subjects of this study were predicted in previous reports to be thermodynamically stable or even experimentally synthesized. Similar to the XH$_6$ system, the XH$_4$ also exhibits a kind of "cage-like" structure. The key distinction lies in the fact that XH$_4$ possesses a tetragonal (*I4/mmm*) structure, incorporating hydrogen molecules but not forming a traditionally complete, closed hydrogen cage. In stark contrast, the structure of XH$_6$ showcases a remarkable body-centered cubic form, with the space group being *Im$\bar{3}$m*, composed solely of metal and hydrogen atoms. It is recognized that pressure-induced formation of hydrogen units can ultimately lead to the emergence of a superconducting state.[10] Referring to Figure 1C, it's notable that upon compression, XH$_4$ and XH$_6$ form

the corresponding H_6 and H_4 units, respectively. Indeed, this unique hydrogen unit structure not only promotes structural stability and metallization but also facilitates superconducting properties.[38] Furthermore, the enhancement of EPC may be observed as the energy level difference within these hydrogen units increases.

Electronic structures

Regarding the electronic properties, our primary focus is on the band that intersects the Fermi energy level. As observed in Figure 1D, MgH_4 exhibits only three bands crossing the Fermi energy level, in contrast to ScH_6, which features six bands intersecting it. The band structures of the other substances are comprehensively detailed in Figure S1. Clearly, in comparison to MgH_4, the band structure of ScH_6 is primarily augmented by several electron pockets. Concurrently, except MgH_6, the band structures of the XH_6 system all exhibit small pockets of electrons converging at the Γ point, manifesting as saddle points. The density of states (DOS) for both XH_4 and XH_6 systems exhibits Van Hove peak singularities, as shown in Figure S2. These singularities are associated with the presence of electron pockets in the band structure. Notably, in the cases of CaH_4 and YH_4, the peaks are predominantly occupied by the d-orbitals of the metal atoms and the s-orbitals of the H2 atoms in conjunction. In contrast, for ScH_4 and MgH_4, the s-orbitals of the H2 atoms play a more dominant role. Therefore, we hypothesize that the specific type of orbitals predominating the peak density of states at the Van Hove singularity position can significantly influence the electronic properties of the material.

To investigate the electronic properties near the Fermi energy level with greater specificity, the 3D Fermi surface and 2D Fermi surface sections of XH_4 and XH_6 are depicted in Figures S3 and S4, respectively. As we can see, many irregular spherical and ribbon-like sheets of FSs exist here along with BZ edges constituting complex FSs for XH_4 as well as XH_6. More specifically, within the XH_4 system, a distinct subdivision into two types of Fermi surfaces (FSs) is observed. This is characterized by spherical FSs centered around the Γ point, predominantly observed in CaH_4 and MgH_4. Conversely, ScH_4 and YH_4 are mainly characterized by a large number of ribbon-like FSs located at the edges of the BZ. However, For the XH_6 system, a common feature is the presence of triangular conical FSs at the boundaries of the BZ. Exceptionally, in CaH_6, ScH_6, and YH_6, there are additional "nesting style" sphere-like FSs centered at the Γ points. This nested spherical FS formation is attributed to the emergence of several electron states in bands that intersect the Fermi energy level. The colors depicted on the FS indicate relative Fermi velocities (v_F). Intriguingly, in all structures except YH_4 and ScH_6, the hole states exhibit higher v_F than the electron pockets, a unique property that may enhance EPC. This part will be focused on in later chapters. Indeed, in general terms, the scope of EPC is typically considered to encompass a small range of shells near the FS as its primary area of influence. Consequently, the size and nature of the FS directly impact the role and effectiveness of EPC. As will be described, alkaline-earth hydrides and rare-earth hydrides exhibit distinctly different natures to the FSs and their EPC mechanism is also markedly divergent.

Phonons

To elucidate the characteristics of crystal vibration more precisely, the phonon dispersion diagrams of MgH_4 and ScH_6 are displayed in Figure 2. The phonon dispersion diagrams for the other substances are available in Figure S5. A notable distinction between the XH_4 and XH_6 systems lies in their hydrogen atom composition. The XH_4 system comprises two types of hydrogen atoms: one derived from a hydrogen molecule and the other being an ordinary hydrogen atom. The investigation reveals that the vibration of the H1 atom, originating from the hydrogen molecule, predominantly contributes to the high-energy zones. This is attributed to the inherently high vibrational frequency of hydrogen molecules. Middle energy zones, mostly be provided by H1 and H2 atoms vibration together. Metal element vibration is contributed to the low-energy zones consisting of three acoustic phonon branches. Peculiarly, the contribution of the metal element in ScH_4 to the medium zones cannot be overlooked. Furthermore, considerable phonon softening is observed along the Γ-X-P paths. Building upon the phonon softening mechanism outlined in prior studies, the EPC constants grow accompanied by the phonon softening, which may elevate the superconducting transition temperature.[50]

Also, as for the XH_6 system, there is only one type hydrogen atom vibration, but it covers almost the entire region of low-medium-high energy. Metal atom vibration still contributes mainly to three low-energy acoustic branches. The phonon softening accompanying the singularity is evident in these systems, which corresponds to the production of electron-hole pairs with a constant overall momentum,[51] and is related to the fact that the radius of curvature of the FSs in the singularity range is larger than the limiting momentum of sphere Fermi surfaces. As mentioned earlier, remarkably, the appearance of the small electron pockets and holes in the Fermi surface in the XH_6. Here, the appearance of phonon softening corresponds to the path where the holes are located. However, the location where appear phonon softening in ScH_6 corresponds to the small electron pockets. Since the phonon softening accompanying the singularity corresponds to a strong electron-phonon interaction, we hypothesize that the phonon softening region will be the chief contributor to the EPC, which may be localized in the small electron pockets near the FS of the ScH_6 structure. This unique phenomenon may impart distinct properties to ScH_6, differentiating it from other structures.

Electron-phonon interactions

The phonon modes that contribute most significantly to the EPC are evident in the phonon linewidth plots displayed in Figures 2, S5, and S6. For the XH_4 system, it is mainly the in-plane vibration of the H2 atom in the xy direction that dominates the EPC. Exceptionally, the out-of-plane vibration of the H1 atoms in the z direction contributes less to the EPC. This differential contribution is attributed to the positioning of the H1 atoms within the hydrogen molecule, which leads to a higher vibrational frequency for these atoms. Unfortunately, it is not guaranteed that all high-frequency phonons are fully thermally excited, which results in a lower participation of these phonons in electron scattering.
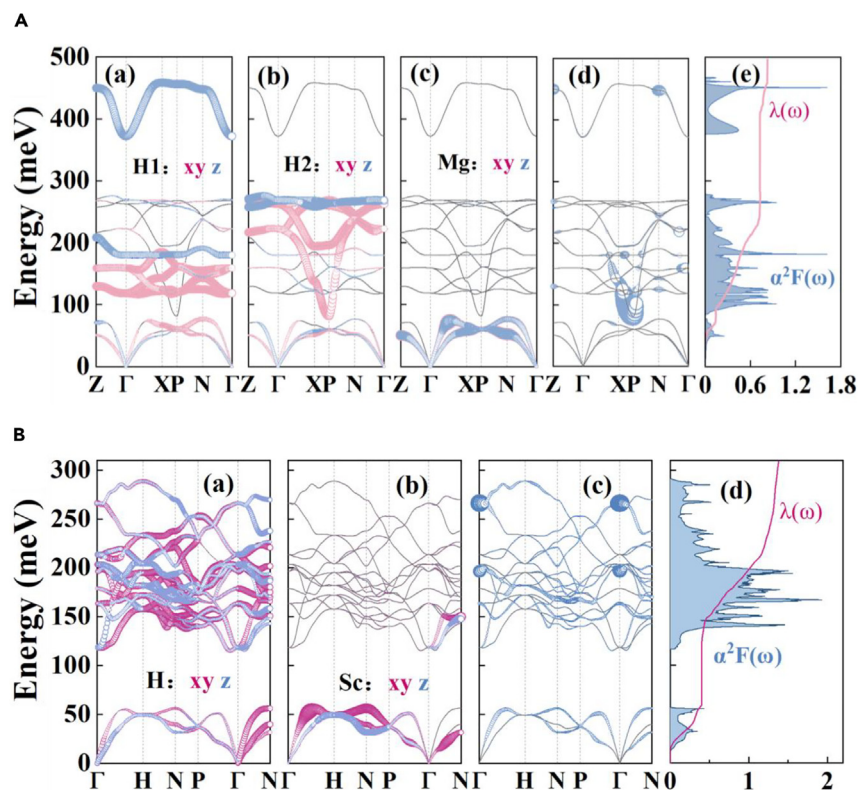
Figure 2. Phonon dispersion and Eliashberg spectral function of MgH$_4$ and ScH$_6$

(A and B) The figures represent MgH$_4$ at 255 GPa and ScH$_6$ at 285 GPa, respectively (a–c) calculate the phonon dispersion diagram of the structure, highlighting the contribution to the different of the elements to the mode. H1 represents atoms in hydrogen molecule and H2 represents the ordinary hydrogen atom. Where red represents in-plane vibration in the xy plane and blue represents the out of plane in the z direction (For ScH$_6$, since there is only one type of hydrogen, the numbering of the properties calculated later is reduced sequentially by one.). (d) Calculated the phonon linewidth and the size of the blue circle is proportional to the amount of λ_{qn} value. (e) Eliashberg spectral function $\alpha^2 F(\omega)$ and $\lambda(\omega)$.

Specifically, in the XH$_4$ system, the electron-phonon interaction is even lower due to the presence of hydrogen molecules. This leads to a reduced concentration of hydrogen ions and consequently a smaller EPC constant λ, which only reaches up to 1.16. In the case of ScH$_4$, the vibration of the Sc atom in the z direction at intermediate frequencies also contributes to the EPC. This specific vibrational mode is a direct factor in the low optical λ of ScH$_4$, with relevant data presented in Table 1. Generally, in the XH$_4$ structure, medium-frequency vibrations along the xy direction, predominantly driven by H2 atoms, are favorable for enhancing the EPC. Interaction with the phonon in the peak region near the Fermi level leads to the softening of the phonon in the middle-frequency band while dominating the EPC. Meanwhile, based on the "phonon softening mechanism,"[50] the reduction in phonon frequency is accompanied by an increase in the λ. This rationally explains why λ_{opt} values are greater than λ_{ac}.

In contrast, the hydrogen atoms in the XH$_6$ structure vibrate in full space to co-dominate the EPC. In this case, the EPC predominantly arises from the Γ points and the region where optical branch softening occurs. Specifically, unlike XH$_4$, the strong interactions between the optical phonon modes due to the high amount of hydrogen ligands in the structure and the electrons belonging to the broadband state culminate in the strong EPC of XH$_6$ as well as the high T_c. It can also be seen by comparing the λ_{ac} and λ_{opt} values between the XH$_4$ and XH$_6$ systems that the total λ in the XH$_6$ system is predominantly influenced by λ_{opt}, attributable to the optical branch EPC contributions from hydrogen. This is the underlying reason for the elevated λ in the XH$_6$ system. Conversely, in the XH$_4$ system, the presence of hydrogen molecules diminishes the value of λ_{opt}, thereby resulting in a comparatively lower total λ value. Here a two-gap model is imported in the XH$_6$ system due to the emergence of the double-peaked DOS near the Fermi energy level. And the extra superconducting gap corresponds to the excitation of small electron pockets. For normal high T_c structures, the difference in momentum between the different bands results in the missing inter-band pairing. However, the existence of a second energy gap creates an extra pairing channel so that pairs within each band must be concerned with the existence of another band, which means that the electrons at the small electron pockets can absorb phonons, and thus inter-band scattering to occurs, with Cooper pairs forming from the small packet of electrons that transition to the vicinity of the bulk Fermi surface. Thus, this reasonably interprets the high T_c and EPC major contribution of CaH$_6$, MgH$_6$, and YH$_6$. The low v_F at the electron pocket and the high v_F corresponding to the phonon softening region of hole states can prove that a large number of electrons are involved in the transport process that occurs in the phonon softening region, which is the main field for EPC to take place. Intriguingly, unlike the other structure, the

Table 1. Electron-phonon coupling constant λ, acoustic branch electron-phonon coupling constant λ_{ac}, optical branch electron-phonon coupling constant λ_{opt}, and superconducting transition temperature T_c for the XH_4 and XH_6 systems

| | Pressure (GPa) | μ^* | This work | | | | Reference |
			λ	λ_{ac}	λ_{opt}	T_c (K)	T_c (K)
CaH_4	160	0.1	0.1	–	–	–	–
MgH_4	255	0.1	0.812	0.115	0.697	84.63	89[41]
		0.12				75	
		0.13				71	
ScH_4	120	0.1	1.142	0.257	0.885	108.4	102-113[52]
		0.12				83	
		0.13				79	
YH_4	120	0.1	1.132	0.217	0.915	92	84-95[53]
		0.12				81	
		0.13				76	
CaH_6	150	0.1	2.628	0.411	2.217	220	235[32]
		0.12				211	
		0.13				206	
MgH_6	300	0.1	2.451	0.362	2.089	255	265[54]
		0.12				245	
		0.13				240	
ScH_6	285	0.1	1.379	0.403	0.976	134	130-147[30]
		0.12				128	
		0.13				124	
YH_6	120	0.1	3.212	0.636	2.576	230	247[32]
		0.12				220	
		0.13				215	

contribution of EPC of ScH_6 is localized in the small electron pocket with high v_F. We hypothesize that strong intraband scattering occurs mainly at the electron pocket thereby generating the Cooper pairs, while it is insensitive to the interband pairing. And the phonon softening is not significant, with a relatively low value of $\lambda = 1.37$.

Superconductivity

Now, focusing on the superconductivity of the XH_4 and XH_6 systems, the Allen-Dynes formula has been utilized to compute the superconducting transition temperature. For these calculations, the empirical parameter μ^* was uniformly set to 0.1–0.13. The reliability of this approach is evidenced by the congruence of our calculated results with previously reported data, as detailed in Table 1. Then, the T_c of the XH_6 system is well above XH_4, where MgH_6 reaches the highest value of 255K. This primarily stems from the strong EPC and the large value of λ. For the traditional BCS formula, both the density of states at Fermi level and the maximum phonon frequency ω_{max} will play a decisive role in the T_c value. Compared with XH_4 and XH_6 systems, the maximum phonon frequency in XH_6 system is generally greater than that in XH_4 system, which is due to the high concentration of H in XH_6 system. With the increase of ω_{max} under pressure, the EPC constant λ strength may be enhanced. However, increasing pressure will significantly weaken the density of states at the Fermi level. For MgH_6, the density of states at Fermi level at 300 GPa is significantly lower than that of other substances (see Figure S2). It can be seen that the change of parameters related to T_c under pressure is very complex. But no direct equations are used in this work to quantitatively describe the relationship between the density of states at the Fermi level and ω_{max} and pressure values respectively, the figures shown in Table 1 are only empirical estimates. We mainly use the superconducting quality factor (S)[55] for each structure to better balance and understand the relationship between applied pressure values and T_c. It is noteworthy that higher values of the quality factor are indicative of superior superconductivity. As illustrated in Figure 3, the majority of the structures exhibit a low-quality factor (less than 1), with only CaH_6 and YH_6 demonstrating values between 1 and 2. Remarkably, YH_6 exhibits a quality factor even larger than the well-known superconductors H_3S and LaH_{10}. This suggests that YH_6 can be considered an exceptionally excellent quality high-temperature superconductor.

Indeed, the phase transition of the charge density wave (CDW) and the superconducting state exhibit a noteworthy correlation. Then, EPC and Fermi-surface Nesting are typically discussed as pivotal factors contributing to the induction of CDW. Here, the calculation of the nesting function, as delineated in Figure 4, demonstrates a pronounced peak at the Γ point for all the structures. The nesting strength in the XH_6 system is notably more pronounced, with the topology of the Fermi strongly nested band can be seen in Figure S4. However, apart from
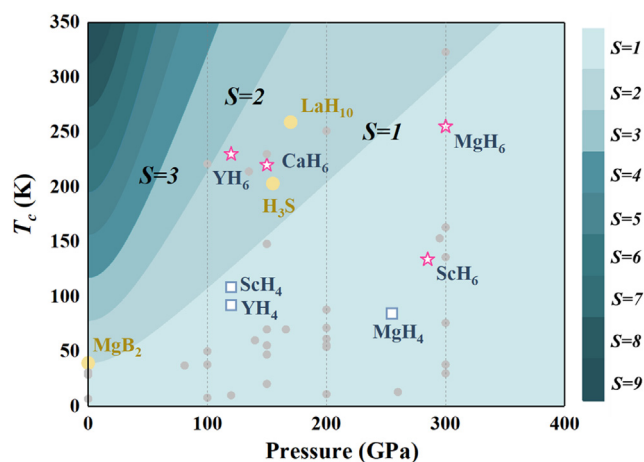
Figure 3. Superconducting quality factor under pressure for each structure
The yellow ball represents the H_3S and LaH_{10} as comparison; square represents the structure of the XH_4 system; red pentagram represents the structure of the XH_6 system and the gray blob represents the structure reported in existing references.

the ScH_6 and CaH_6 structures, the contributions to EPC have primarily concentrated in the phonon softening regions outside the Γ point. This gives us the insight that for the XH_4 and XH_6 structure, further consideration of momentum-dependent EPC is needed to explain the phonon softening as well as the origin of the CDW,[56] particularly for ScH_6 and CaH_6, mainly as a result of strong Fermi surface nesting. Subsequently, the CDW transition is discussed next. The phonon softening brought about structure instability, the CDW transition occurs when the temperature falls below T_{CDW}, energy gap opens up near the Fermi energy level. Here, in addition to MgH_4 and MgH_6, the exotic sight of saddle-point nesting occurs in the XH_4 and XH_6 systems. The interband transition in states approaching the saddle point is strengthened. This demonstrates that the energy gap modifies the quasiparticle scattering in its bands with saddle points close to the Fermi energy level, and with the forming of an energy gap, the DOS at the saddle point decreases and shifts to form the energy gap. The peak of the DOS value at the saddle point near the Fermi energy level is observed to be low. This observation suggests a close association between saddle-point nesting and the CDW transition. Consequently, the primary factor dominating the CDW order may be the underlying cause of the differing superconducting mechanisms in the XH_4 and XH_6 systems.

d-orbital effects

As previously noted, the hole states and the electronic states formed at the Fermi surface by the bands intersecting the Fermi energy levels serve as the principal sites for EPC. In Figure 5, we present the contributions of different orbitals in each structure to the hole state and the electronic state. Here, the presence or absence of d-orbital electrons outside the nucleus of metallic elements is considered as a key differentiating factor. Firstly, for MgH_n (n = 4,6), the EPC predominantly originates from the interaction between electron transport and phonon softening regions. These regions include extensive areas of hole states characterized by high v_F at the Fermi surface. It is noteworthy that the s-orbital electrons of H in MgH_6 dominate the hole states and the DOS peak near the Fermi energy level is essentially provided by the s-orbital of H (Figure S2), which is a direct factor leading to its high T_c. Meanwhile, for structures with d-orbital electrons involved, the saddle-point nesting spectacle occurs at Γ points, which echoes the calculation of the nesting function. We believe that the involvement of d-orbital electrons is the key to saddle-point nesting. Among them, ScH_4 and YH_4, the DOS peaks at the saddle points are provided by both H-1s orbitals and metal element-d orbitals (see Figures S2 and S7), and the Fermi surface consists of a large area of blanket-like hole states, the d-orbital of metallic elements and H-1s orbital electrons are involved in electron transport and EPC. However, the presence of hydrogen molecules in the structure rather reduces the H concentration in the structure. As a consequence, the participation of d-orbital electrons from metal elements becomes more dominant in the EPC process, which suppresses its T_c.

Shifting our focus to the XH_6 system, we particularly concentrate on the high T_c structure of YH_6. In this case, the H-1s orbitals have the largest share of the Fermi surface, followed by the Y-d orbitals. For the saddle point, the excitation of electrons at small electron pockets is mainly considered, and with the increase of scattering intensity, interband scattering occurs and transitions to a large Fermi surface (hole) to form a Cooper pair. In addition, for the hole states with high v_F corresponding to the phonon softening region, there are three types of Y-d orbitals, namely, A_1' (d_{z^2}), E' (d_{xy,x^2-y^2}), and E'' ($d_{xz,yz}$). Derived from the idea of doping, the addition of Y-4d holes moves toward the hole conduction of the ligand H-1s. Its ligand hole wave function is regarded as a linear combination of the H-1s orbitals with several d orbitals mentioned above, which ultimately completes the exchange coupling between Y-4d and H-1s holes in the phonon softening region. Due to the combination with the high-energy state Y-4d holes, the lowest energy hole single-line state is reached. This is the essential reason why YH_6 reaches T_c values as high as 230 K, quite different from MgH_6.

In the case of ScH_6, the CDW order is primarily attributed to Fermi surface nesting. The 3D Fermi surface analysis reveals that the second band crossing the Fermi surface exhibits both hole and electron characteristics. However, these two structures are "sticky," as seen in Figure S8.
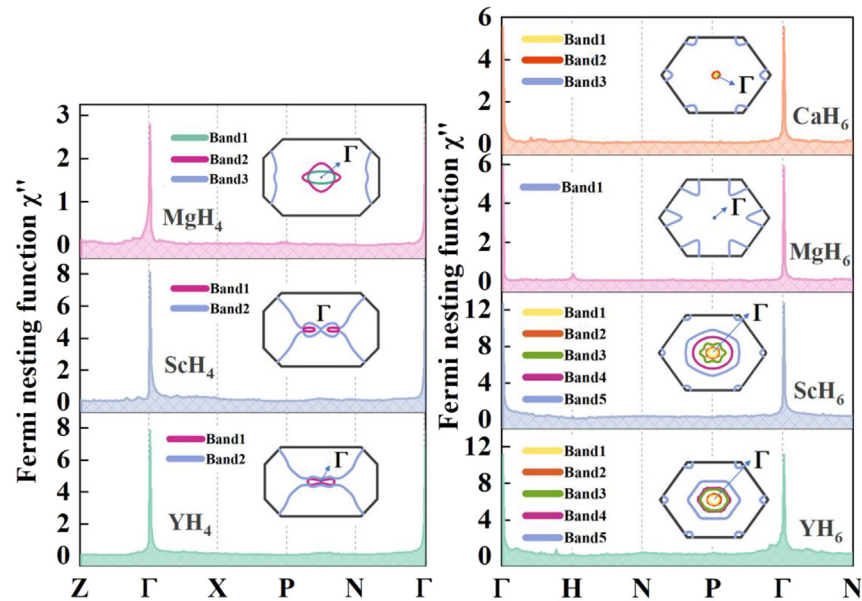
Figure 4. Calculated Fermi nesting function of XH$_4$ and XH$_6$ (X = Ca, Mg, Sc, and Y; Since CaH$_4$ in the *I4/mmm* phase was calculated not to be superconducting, its nesting function was not calculated), the small figure in the upper right corner shows the section of the Fermi surface in the 111 direction, with the different colors representing the different bands passing through the Fermi energy

This "stickiness" implies that the hole and electron states are intimately connected, forming a closed state. Additionally, the partial DOS (PDOS) peak of H-1s has a deviation distance from the total DOS (TDOS) and Y-3d peaks. We hypothesize that this special interaction leads to a severe interference of the hole with the electron pocket, which prevents Sc-3d and H-1s holes from coupling. This is related to the influence of the periodic potential field on the electrons, as the high-ionization energy of the metal element Sc leads to a strong binding effect of the extra-nuclear electrons by the periodic potential field. Consequently, in the case of ScH$_6$, the electronic and hole structures uniquely exhibit this pronounced interference effect, where they are completely interconnected. This scenario, combined with the fact that most of the EPC in ScH$_6$ is localized within small electron pockets and does not extend to larger areas of the Fermi surface, results in a relatively lower T_c of only 133 K.

Conclusion

In conclusion, our study delved into the electronic structure, EPC, and superconductivity of alkaline-earth and rare-earth metal hydrides XH$_n$ (n = 4,6). We found that the presence of hydrogen molecules in XH$_4$ results in a lower concentration of hydrogen ions, which correlates with lower superconducting transition temperatures. The highest T_c recorded within this group was 108.4 K for ScH$_4$. For structures where d-orbital electrons participate in the electron-phonon interaction, a double-gap model was introduced for CaH$_6$, ScH$_6$, and YH$_6$. In this model, an additional superconducting gap corresponds to the excitation of a small pocket of electrons. Our analysis of the superconducting quality factor and CDW order revealed that the CDW order in YH$_6$ is induced by strong EPC. Furthermore, YH$_6$ exhibits an exceptional superconducting
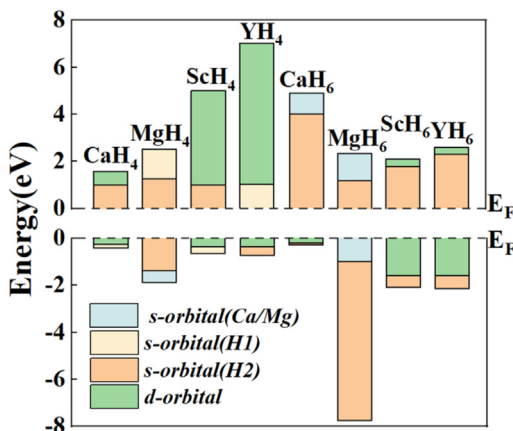

Figure 5. Divided into two parts using the Fermi energy level as the dividing line, above the Fermi energy level represents the hole structure corresponding to the Fermi surface, and below the Fermi energy level represents the electronic structure

The total height of the cylinder represents the cross distance of the highest/lowest point of the band from the Fermi energy level. The different colors and corresponding cylindrical heights represent the different orbitals of XH$_4$ and XH$_6$ (X = Ca, Mg, Sc, and Y) and their contributions to the hole structure/electron structure partial bands, respectively. Where H1 represents atoms in the hydrogen molecule and H2 represents ordinary hydrogen atoms.

quality factor, close to 2, positioning it as an outstanding high-temperature superconductor due to its strong EPC-induced CDW order. Ultimately, we propose an innovative rule for high-temperature superconductivity: the presence of a double gap, with EPC predominantly concentrated in phonon softening regions involving high-energy states and H-1s hole couplings. This rule suggests that rare-earth elements with lower ionization energies could form high T_c hydrides, paving the way for discovering efficient superconducting materials.

Limitations of the study

This study provides valuable insights into the electronic structure, EPC and superconductivity of alkaline-earth and rare-earth metal hydrides (XH_n, $n = 4,6$). However, limitations include the need for further experimental validation of hydrogen ion concentrations' direct impact on superconducting transition temperatures, refinement of EPC models for accurate T_c predictions across diverse hydride systems, and broader validation of proposed rules linking double gaps and EPC-induced CDW order to high-temperature superconductivity. Addressing these limitations will enhance our understanding and application of these materials in superconducting technologies.

STAR★METHODS

Detailed methods are provided in the online version of this paper and include the following:

- KEY RESOURCES TABLE
- RESOURCE AVAILABILITY
  - Lead contact
  - Materials availability
  - Data and code availability
- EXPERIMENTAL MODEL AND STUDY PARTICIPANT DETAILS
- METHOD DETAILS
  - Specific methods
  - Electronic structure calculations
  - Phonon calculations and electron-phonon coupling (EPC)
  - CDW analysis
- QUANTIFICATION AND STATISTICAL ANALYSIS
- ADDITIONAL RESOURCES

SUPPLEMENTAL INFORMATION

Supplemental information can be found online at https://doi.org/10.1016/j.isci.2024.110542.

AUTHOR CONTRIBUTIONS

Y.-L.T. developed the outline, researched resources, and led the drafting and editing of the manuscript. D.-H.F., F.-S.L., and Z.-T.L. provided strategic input and supported the writing and editing process. Q.-J.L. conceptualized the publication and provided strategic oversight and editing.

DECLARATION OF INTERESTS

The authors declare no competing interests.

REFERENCES

1. McMahon, J.M., and Ceperley, D.M. (2011). Ground-state structures of atomic metallic hydrogen. Phys. Rev. Lett. *106*, 165302. https://doi.org/10.1103/PhysRevLett.106.165302.

2. Azadi, S., Monserrat, B., Foulkes, W.M.C., and Needs, R.J. (2014). Dissociation of high-pressure solid molecular hydrogen: a quantum monte carlo and anharmonic vibrational study. Phys. Rev. Lett. *112*, 165501. https://doi.org/10.1103/PhysRevLett.112.165501.

3. Zha, C.s., Liu, Z., Ahart, M., Boehler, R., and Hemley, R.J. (2013). High-pressure measurements of hydrogen phase iv using synchrotron infrared spectroscopy. Phys. Rev. Lett. *110*, 217402. https://doi.org/10.1103/PhysRevLett.110.217402.

4. Loubeyre, P., Occelli, F., and Letoullec, R. (2002). Optical studies of solid hydrogen to 320 gpa and evidence for black hydrogen. Nature *416*, 613–617. https://doi.org/10.1038/416613a.

5. Goncharov, A.F., Tse, J.S., Wang, H., Yang, J., Struzhkin, V.V., Howie, R.T., and Gregoryanz, E. (2013). Bonding, structures, and band gap

closure of hydrogen at high pressures. Phys. Rev. B *87*, 024101. https://doi.org/10.1103/PhysRevB.87.024101.

6. McMinis, J., Clay, R.C., Lee, D., and Morales, M.A. (2015). Molecular to atomic phase transition in hydrogen under high pressure. Phys. Rev. Lett. *114*, 105305. https://doi.org/10.1103/PhysRevLett.114.105305.

7. Song, X., Liu, C., Li, Q., Hemley, R.J., Ma, Y., and Chen, C. (2022). Stress-induced high-T_c superconductivity in solid molecular hydrogen. Proc. Natl. Acad. Sci. USA *119*, e2122691119. https://doi.org/10.1073/pnas.2122691119.

8. Ashcroft, N.W. (2004). Hydrogen dominant metallic alloys: high temperature superconductors? Phys. Rev. Lett. *92*, 187002. https://doi.org/10.1103/PhysRevLett.92.187002.

9. Sun, Y., Zhong, X., Liu, H., and Ma, Y. (2024). Clathrate metal superhydrides under high-pressure conditions: enroute to room-temperature superconductivity. Natl. Sci. Rev. *11*, nwad270. https://doi.org/10.1093/nsr/nwad270.

10. Wang, H., Tse, J.S., Tanaka, K., Iitaka, T., and Ma, Y. (2012). Superconductive sodalite-like clathrate calcium hydride at high pressures. Proc. Natl. Acad. Sci. USA *109*, 6463–6466. https://doi.org/10.1073/pnas.1118168109.

11. Wang, K., Xie, Y., Yang, X., Wang, Y., Zhou, M., Liu, H., Yu, X., Zhao, Y., Wang, H., Liu, G., et al. (2022). High-temperature superconducting phase in clathrate calcium hydride ${\mathrm{cah}}_{6}$ up to 215 k at a pressure of 172 gpa. Phys. Rev. Lett. *128*, 167001. https://doi.org/10.1103/PhysRevLett.128.167001.

12. Duan, D., Liu, Y., Tian, F., Li, D., Huang, X., Zhao, Z., Yu, H., Liu, B., Tian, W., and Cui, T. (2014). Pressure-induced metallization of dense (h2s)2h2 with high-tc superconductivity. Sci. Rep. *4*, 6968. https://doi.org/10.1038/srep06968.

13. Drozdov, A.P., Eremets, M.I., Troyan, I.A., Ksenofontov, V., and Shylin, S.I. (2015). Conventional superconductivity at 203 kelvin at high pressures in the sulfur hydride system. Nature *525*, 73–76. https://doi.org/10.1038/nature14964.

14. Liu, H., Naumov, I.I., Hoffmann, R., Ashcroft, N.W., and Hemley, R.J. (2017). Potential high-tc superconducting lanthanum and yttrium hydrides at high pressure. Proc. Natl. Acad. Sci. USA *114*, 6990–6995. https://doi.org/10.1073/pnas.1704505114.

15. Drozdov, A.P., Kong, P.P., Minkov, V.S., Besedin, S.P., Kuzovnikov, M.A., Mozaffari, S., Balicas, L., Balakirev, F.F., Graf, D.E., Prakapenka, V.B., et al. (2019). Superconductivity at 250 k in lanthanum hydride under high pressures. Nature *569*, 528–531. https://doi.org/10.1038/s41586-019-1201-8.

16. Si, J., Turnbull, R., Liang, A., Liu, P., Wang, B., and Shi, L. (2024). Prediction of pressure-induced superconductivity in the ternary systems ${\mathrm{ysch}}_{2n}$ ($n=3$–6). Phys. Rev. B *109*, 54512. https://doi.org/10.1103/PhysRevB.109.054512.

17. Tu, X.H., Bo, T., Liu, P.F., Yin, W., Hao, N., and Wang, B.T. (2022). Superconductivity in mo–p compounds under pressure and in double-weyl semimetal hex-mop2. Phys. Chem. Chem. Phys. *24*, 7893–7900. https://doi.org/10.1039/D1CP05685A.

18. Chen, L.C., Luo, T., Cao, Z.Y., Dalladay-Simpson, P., Huang, G., Peng, D., Zhang, L.L., Gorelli, F.A., Zhong, G.H., Lin, H.Q., and Chen, X.J. (2024). Synthesis and superconductivity in yttrium-cerium hydrides at high pressures. Nat. Commun. *15*, 1809. https://doi.org/10.1038/s41467-024-46133-x.

19. Shutov, G.M., Semenok, D.V., Kruglov, I.A., and Oganov, A.R. (2024). Ternary superconducting hydrides in the la–mg–h system. Mater. Today Phys. *40*, 101300. https://doi.org/10.1016/j.mtphys.2023.101300.

20. Wang, J., Sun, Y., Li, Y., Zhang, S., Gao, B., and Liu, H. (2023). High-tc superconductivity of polyhydride rb2mgh18 with a layered hydrogen structure at high pressure. J. Mater. Chem. C *11*, 14755–14762. https://doi.org/10.1039/D3TC02427J.

21. Minkov, V.S., Bud Ko, S.L., Balakirev, F.F., Prakapenka, V.B., Chariton, S., Husband, R.J., Liermann, H.P., and Eremets, M.I. (2022). Magnetic field screening in hydrogen-rich high-temperature superconductors. Nat. Commun. *13*, 3194. https://doi.org/10.1038/s41467-022-30782-x.

22. Ding, X., Tam, C.C., Sui, X., Zhao, Y., Xu, M., Choi, J., Leng, H., Zhang, J., Wu, M., Xiao, H., et al. (2023). Critical role of hydrogen for superconductivity in nickelates. Nature *615*, 50–55. https://doi.org/10.1038/s41586-022-05657-2.

23. Morimachi, Y., Urai, M., Nakajima, R., Kamebuchi, H., Miyagawa, K., Kanoda, K., and Zhou, B. (2023). An organic superconductor, (tea)(hedo-ttf-dc)2·2(h2c2o4), coupled with strong hydrogen-bonding interactions. Chem. Commun. *59*, 4162–4165. https://doi.org/10.1039/D3CC00080J.

24. Gao, M., Guo, P.J., Yang, H.C., Yan, X.W., Ma, F., Lu, Z.Y., Xiang, T., and Lin, H.Q. (2023). Stabilizing a hydrogen-rich superconductor at 1 gpa by charge transfer modulated virtual high-pressure effect. Phys. Rev. B *107*, L180501. https://doi.org/10.1103/PhysRevB.107.L180501.

25. Zhang, Z., Cui, T., Hutcheon, M.J., Shipley, A.M., Song, H., Du, M., Kresin, V.Z., Duan, D., Pickard, C.J., and Yao, Y. (2022). Design principles for high-temperature superconductors with a hydrogen-based alloy backbone at moderate pressure. Phys. Rev. Lett. *128*, 047001. https://doi.org/10.1103/PhysRevLett.128.047001.

26. Osmond, I., Moulding, O., Cross, S., Muramatsu, T., Brooks, A., Lord, O., Fedotenko, T., Buhot, J., and Friedemann, S. (2022). Clean-limit superconductivity in $im\overline{3}m {\mathrm{h}}_{3}\mathrm{s}$ synthesized from sulfur and hydrogen donor ammonia borane. Phys. Rev. B *105*, L220502. https://doi.org/10.1103/PhysRevB.105.L220502.

27. Salke, N.P., Davari Esfahani, M.M., Zhang, Y., Kruglov, I.A., Zhou, J., Wang, Y., Greenberg, E., Prakapenka, V.B., Liu, J., Oganov, A.R., and Lin, J.F. (2019). Synthesis of clathrate cerium superhydride ceh9 at 80-100 gpa with atomic hydrogen sublattice. Nat. Commun. *10*, 4453. https://doi.org/10.1038/s41467-019-12326-y.

28. Semenok, D.V., Kvashnin, A.G., Ivanova, A.G., Svitlyk, V., Fominski, V.Y., Sadakov, A.V., Sobolevskiy, O.A., Pudalov, V.M., Troyan, I.A., and Oganov, A.R. (2020). Superconductivity at 161 k in thorium hydride thh10: synthesis and properties. Mater. Today Off. *33*, 36–44. https://doi.org/10.1016/j.mattod.2019.10.005.

29. Zhou, D., Semenok, D.V., Duan, D., Xie, H., Chen, W., Huang, X., Li, X., Liu, B., Oganov, A.R., and Cui, T. (2020). Superconducting praseodymium superhydrides. Sci. Adv. *6*, eaax6849. https://doi.org/10.1126/sciadv.aax6849.

30. Abe, K. (2017). Hydrogen-rich scandium compounds at high pressures. Phys. Rev. B *96*, 144108. https://doi.org/10.1103/PhysRevB.96.144108.

31. Chen, W., Semenok, D.V., Kvashnin, A.G., Huang, X., Kruglov, I.A., Galasso, M., Song, H., Duan, D., Goncharov, A.F., Prakapenka, V.B., et al. (2021). Synthesis of molecular metallic barium superhydride: pseudocubic bah12. Nat. Commun. *12*, 273. https://doi.org/10.1038/s41467-020-20103-5.

32. Tanaka, K., Tse, J.S., and Liu, H. (2017). Electron-phonon coupling mechanisms for hydrogen-rich metals at high pressure. Phys. Rev. B *96*, 100502. https://doi.org/10.1103/PhysRevB.96.100502.

33. Xie, H., Yao, Y., Feng, X., Duan, D., Song, H., Zhang, Z., Jiang, S., Redfern, S.A.T., Kresin, V.Z., Pickard, C.J., and Cui, T. (2020). Hydrogen pentagraphenelike structure stabilized by hafnium: a high-temperature conventional superconductor. Phys. Rev. Lett. *125*, 217001. https://doi.org/10.1103/PhysRevLett.125.217001.

34. Lonie, D.C., Hooper, J., Altintas, B., and Zurek, E. (2013). Metallization of magnesium polyhydrides under pressure. Phys. Rev. B *87*, 054107. https://doi.org/10.1103/PhysRevB.87.054107.

35. Du, M., Zhang, Z., Song, H., Yu, H., Cui, T., Kresin, V.Z., and Duan, D. (2021). High-temperature superconductivity in transition metallic hydrides mh11 (m = mo, w, nb, and ta) under high pressure. Phys. Chem. Chem. Phys. *23*, 6717–6724. https://doi.org/10.1039/D0CP06435A.

36. Liu, L., Wang, C., Yi, S., Kim, K.W., Kim, J., and Cho, J.H. (2019). Microscopic mechanism of room-temperature superconductivity in compressed ${\mathrm{lah}}_{10}$. Phys. Rev. B *99*, 140501. https://doi.org/10.1103/PhysRevB.99.140501.

37. Semenok, D.V., Song, H., Szczęśniak, R., Wrona, I.A., Akashi, R., Davari Esfahani, M.M., Duan, D., Cui, T., Kvashnin, A.G., Oganov, A.R., and Kruglov, I.A. (2020). Superconductivity of ${\mathrm{lah}}_{10}$ and ${\mathrm{lah}}_{16}$ polyhydrides. Phys. Rev. B *101*, 24508. https://doi.org/10.1103/PhysRevB.101.024508.

38. Tao, Y.L., Zeng, W., Gao, J., Liu, Z.T., Jiao, Z., and Liu, Q.J. (2023). Composition and structural characteristics of compressed alkaline earth metal hydrides. Phys. Chem. Chem. Phys. *25*, 26225–26235. https://doi.org/10.1039/D3CP03134A.

39. Wu, G., Huang, X., Xie, H., Li, X., Liu, M., Liang, Y., Huang, Y., Duan, D., Li, F., Liu, B., and Cui, T. (2019). Unexpected calcium polyhydride cah4: a possible route to dissociation of hydrogen molecules. J. Chem. Phys. *150*, 044507. https://doi.org/10.1063/1.5053650.

40. Shao, Z., Duan, D., Ma, Y., Yu, H., Song, H., Xie, H., Li, D., Tian, F., Liu, B., and Cui, T. (2019). Unique phase diagram and superconductivity of calcium hydrides at high pressures. Inorg. Chem. *58*, 2558–2564. https://doi.org/10.1021/acs.inorgchem.8b03165.

41. Abe, K. (2018). High-pressure properties of dense metallic zirconium hydrides studied by ab initio calculations. Phys. Rev. B *98*, 134103. https://doi.org/10.1103/PhysRevB.98.134103.

42. Sheng, X., Yan, X., Chen, Y., Song, B., and Qian, S. (2017). Theoretical study of stability and superconductivity of ${\mathrm{sch}}_{n}$ ($n=4–8$) at high pressure. Phys. Rev. B *96*, 94513. https://doi.org/10.1103/PhysRevB.96.094513.

43. Giannozzi, P., Baroni, S., Bonini, N., Calandra, M., Car, R., Cavazzoni, C., Ceresoli, D., Chiarotti, G.L., Cococcioni, M., Dabo, I., et al. (2009). Quantum espresso: a modular and open-source software project for quantum simulations of materials. J. Phys. Condens. Matter *21*, 395502. https://doi.org/10.1088/0953-8984/21/39/395502.

44. Giannozzi, P., Andreussi, O., Brumme, T., Bunau, O., Buongiorno Nardelli, M., Calandra, M., Car, R., Cavazzoni, C., Ceresoli, D., Cococcioni, M., et al. (2017). Advanced capabilities for materials modelling with quantum espresso. J. Phys. Condens. Matter *29*, 465901. https://doi.org/10.1088/1361-648X/aa8f79.

45. Giannozzi, P., Baseggio, O., Bonfà, P., Brunato, D., Car, R., Carnimeo, I., Cavazzoni, C., de Gironcoli, S., Delugas, P., Ferrari Ruffino, F., et al. (2020). Quantum espresso toward the exascale. J. Chem. Phys. *152*, 154105. https://doi.org/10.1063/5.0005082.

46. Hamann, D.R. (2013). Optimized norm-conserving vanderbilt pseudopotentials. Phys. Rev. B *88*, 085117. https://doi.org/10.1103/PhysRevB.88.085117.

47. Baroni, S., de Gironcoli, S., Dal Corso, A., and Giannozzi, P. (2001). Phonons and related crystal properties from density-functional perturbation theory. Rev. Mod. Phys. *73*, 515–562. https://doi.org/10.1103/RevModPhys.73.515.

48. Allen, P.B. (1972). Neutron spectroscopy of superconductors. Phys. Rev. B *6*, 2577–2579. https://doi.org/10.1103/PhysRevB.6.2577.

49. Giustino, F. (2017). Electron-phonon interactions from first principles. Rev. Mod. Phys. *89*, 015003. https://doi.org/10.1103/RevModPhys.89.015003.

50. Mcmillan, W.L. (1968). Transition temperature of strong-coupled superconductors. Phys. Rev. *167*, 331–344. https://doi.org/10.1103/PhysRev.167.331.

51. Afanas'Ev, A.A.K.Y. (1963). Singularities caused by electron-phonon interaction in the phonon dispersion law. Sov. Phys. - JETP *16*.

52. Bi, T., and Zurek, E. (2021). Electronic structure and superconductivity of compressed metal tetrahydrides. Chem. Eur J. *27*, 14858–14870. https://doi.org/10.1002/chem.202102679.

53. Li, Y., Hao, J., Liu, H., Tse, J.S., Wang, Y., and Ma, Y. (2015). Pressure-stabilized superconductive yttrium hydrides. Sci. Rep. *5*, 9948. https://doi.org/10.1038/srep09948.

54. Feng, X., Zhang, J., Gao, G., Liu, H., and Wang, H. (2015). Compressed sodalite-like mgh6 as a potential high-temperature superconductor. RSC Adv. *5*, 59292–59296. https://doi.org/10.1039/C5RA11459D.

55. Song, H., Zhang, Z., Cui, T., Pickard, C.J., Kresin, V.Z., and Duan, D. (2021). High tc superconductivity in heavy rare earth hydrides. Chin. Phys. Lett. *38*, 107401. https://doi.org/10.1088/0256-307X/38/10/107401.

56. Yan, L., Si, J., Zhu, S., Wang, B., Wei, Y., Pang, K., Li, W., Zhou, L., and Ku, R. (2023). Ab initio investigation of charge density wave and superconductivity in two-dimensional janus $2h/1t$-mosh monolayers. Phys. Rev. B *107*, 64508. https://doi.org/10.1103/PhysRevB.107.064508.

STAR★METHODS

KEY RESOURCES TABLE

REAGENT or RESOURCE	SOURCE	IDENTIFIER
All analyzed data	This Study	

RESOURCE AVAILABILITY

Lead contact

Further information and requests for resources should be directed to the lead contact, Qi-Jun Liu (E-mail: qijunliu@home.swjtu.edu.cn).

Materials availability

This study did not generate new unique reagents.

Data and code availability

- All data reported in this paper will be shared by the lead contact upon request.
- This paper does not report original code.
- Any additional information required to reanalyze the data reported in this paper is available from the lead contact upon request.

EXPERIMENTAL MODEL AND STUDY PARTICIPANT DETAILS

No experimental model and participant in this study.

METHOD DETAILS

Specific methods

The calculations were conducted using the plane wave pseudopotential method implemented in the QUANTUM ESPRESSO package. To simulate the electron-ion interactions, we employed optimized norm-conserving Vanderbilt pseudopotentials (ONCVPSP). The exchange and correlation potential were described using the generalized gradient approximation (GGA-PBE). We set the wave function cutoff energy to 100 Ry and the charge density cutoff energy to 400 Ry. For Brillouin zone integrations, we utilized a $36 \times 36 \times 36$ k-point mesh with Gaussian smearing of 0.02 Ry. The internal atomic positions were fully relaxed until the forces converged to a critical value of 10 meV/Å. To estimate Fermi surfaces (FSs) and visualize the results, we used Wannier90 interpolation, followed by visualization with the FERMISURFER software. The phonon dispersion and electron-phonon coupling (EPC) calculations were based on density functional perturbation theory (DFPT) and were performed using a $9 \times 9 \times 9$ q-point grid.

Electronic structure calculations

(1) Density Functional Theory (DFT) calculations were performed using Quantum ESPRESSO.
(2) The electronic structure was calculated with a plane-wave basis set and an energy cutoff of 100 eV.
(3) A Monkhorst-Pack k-point mesh of $36 \times 36 \times 36$ was used for Brillouin zone integration.

Phonon calculations and electron-phonon coupling (EPC)

(1) Phonon calculations were conducted using Density Functional Perturbation Theory (DFPT).
(2) Electron-phonon coupling (EPC) was analyzed using the Eliashberg spectral function, and the electron-phonon coupling constant, λ.
(3) The superconducting transition temperature (T_c) was estimated using the McMillan-Allen-Dynes formula.

CDW analysis

(1) The presence of the charge density wave (CDW) phase was determined by inspecting the Fermi surface and identifying saddle-point nesting.
(2) Superconducting gaps were calculated and analyzed for double-gap features, particularly in systems involving d-orbital electrons (e.g., CaH_6, ScH_6, and YH_6).

All computational parameters and methods were selected to optimize the balance between computational cost and accuracy. Results were carefully validated by comparing the calculated values with experimental data where available.

QUANTIFICATION AND STATISTICAL ANALYSIS

Superconducting properties were quantified using Density Functional Theory (DFT) calculations with Quantum ESPRESSO. Electronic structures were calculated with a plane-wave basis set and a [specify energy cutoff, e.g., 100 eV] energy cutoff, using a Monkhorst-Pack k-point mesh of [specify grid density, e.g., 36 × 36 × 36]. Phonon calculations were conducted using density functional perturbation theory (DFPT), and electron-phonon coupling (EPC) was analyzed via the Eliashberg function and coupling constant λ. The superconducting transition temperature (T_c) was estimated using the McMillan-Allen-Dynes formula. Calculations were repeated for convergence and reproducibility, with key parameters validated against published data. Charge density wave (CDW) phases and superconducting gaps were analyzed, particularly in systems with d-orbital electrons (e.g., CaH_6, ScH_6, YH_6). All computational parameters and methods were optimized for accuracy and validated with experimental data where available.

ADDITIONAL RESOURCES

Additional resources, including supplementary data, computational codes, and detailed methodological protocols, are available upon request from the lead contact. All supplementary materials are intended to enhance the reproducibility and transparency of the study, providing comprehensive insights into the experimental and computational approaches employed. For access to these resources, please contact [lead contact, Qi-Jun Liu (E-mail: qijunliu@home.swjtu.edu.cn)]. The supplementary data include raw and processed data files, input files for computational simulations, and step-by-step protocols for the methodologies described in this study. These resources aim to support further research and validation efforts within the scientific community.